Environmental Science Nano

ROYAL SOCIETY OF CHEMISTRY

PAPER

Cite this: *Environ. Sci.: Nano*, 2025, 12, 4684

Non-radical oxidation of TBBPA and TBBPS in soil using Fe and Cu co-doped sulfurized carbon nitride: a comparative study of peroxymonosulfate and peroxydisulfate activation

Qi Wang,[ab] Xuewen Guo,[a] Aiguo Gu,[b] Hongzhen Lian *[a] and Jie Zou*[b]

Received 2nd July 2025,
Accepted 5th September 2025

DOI: 10.1039/d5en00600g

rsc.li/es-nano

The non-radical oxidation pathways in persulfate-based advanced oxidation processes (PS-AOPs) offer significant potential for soil and groundwater remediation. However, the construction of non-radical systems and the underlying reaction mechanisms remain insufficiently understood. In this study, Fe and Cu co-doped sulfurized carbon nitride (FeCuS@GFs) was distributed on the surface of graphite felt for non-radical oxidation pathways. FeCuS@GFs activated peroxydisulfate (PDS) and peroxymonosulfate (PMS) to generate an electron transfer process and Fe(IV) active species as the primary non-radical oxidation pathways, respectively. FeCuS@GFs exhibited high efficiency in removing tetrabromobisphenol A (TBBPA) and tetrabromobisphenol S (TBBPS) from aqueous matrices. Comparative analysis demonstrated that Fe(IV) active species exhibited higher reactivity than the electron transfer process for degrading TBBPA/S. Density functional theory (DFT) calculations and experiments further revealed that TBBPS was more resistant to non-radical oxidation than TBBPA. Additionally, soil properties, including pH, Fe-containing minerals and organic matter, influenced the efficiency of electron transfer processes and Fe(IV) active species. The FeCuS@GFs/PMS system achieved nearly complete removal of TBBPA/S from various soil samples, highlighting its superior applicability for soil and groundwater remediation. This study provides novel insights into the role of non-radical oxidation pathways and their potential for actual soil and groundwater treatment.

Environmental significance

Non-radical oxidation pathways could selectively degrade electron-rich pollutants and are resistant to conventional radical quenchers. However, the reaction mechanisms and influencing factors in actual soil and groundwater remediation remain unclear. This work advances the understanding of non-radical oxidation pathways in persulfate-based advanced oxidation processes and provides valuable insights into their application for the removal of persistent organic pollutants from soil and groundwater.

1. Introduction

Brominated flame retardants (BFRs) are a class of artificial organic compound widely used to reduce material flammability in plastics, electronics, and construction materials.[1] Tetrabromobisphenol A (TBBPA) was one of the most widely used BFRs.[2] Due to its resistance to chemical and microbial degradation, TBBPA has been classified as a persistent organic pollutant (POP). TBBPA has been demonstrated to cause developmental toxicity,[3] neurotoxicity,[4] and cytotoxicity.[5] The International Agency for Research on Cancer (IARC) of the World Health Organization (WHO) has classified TBBPA as a Group 2A carcinogen, highlighting the urgent need to limit its use. Therefore, tetrabromobisphenol S (TBBPS) was gradually being used in industrial production as an alternative to TBBPA.[6] However, the widespread presence of TBBPA and TBBPS in environmental and biological samples[7,8] raises significant concerns regarding their effective removal, particularly in soil and groundwater systems.

Persulfate-based advanced oxidation processes (PS-AOPs) have emerged as a promising technology for soil and groundwater remediation. The removal mechanisms of pollutants in PS-AOPs are categorized into free radical and non-

[a] *State Key Laboratory of Analytical Chemistry for Life Science, School of Chemistry and Chemical Engineering and Center of Materials Analysis, Nanjing University, Nanjing 210023, China. E-mail: hzlian@nju.edu.cn*
[b] *Key Laboratory of Food Contact Materials Safety, Jiangsu Product Quality Testing and Inspection Institute, Nanjing, Jiangsu 210007, China. E-mail: 13951700473@139.com*

radical oxidation pathways. Free radical oxidation pathways involve hydroxyl radicals (·OH) and sulfate radicals ($SO_4^{\cdot-}$), whereas non-free radical oxidation pathways include singlet oxygen ($^1O_2$), high-valent metal active species, and electron transfer processes.[9] The free radical oxidation pathway possesses strong mineralization capabilities and is highly effective in removing organic pollutants.[10] However, the free radical oxidation pathway lacks selectivity, and organic matter and inorganic anions can significantly inhibit its removal of pollutants.[11] Under certain specific conditions, the free radical oxidation pathway can produce halogenated disinfection by-products,[12] causing secondary pollution. Compared to the free radical oxidation pathway, the greatest advantage of the non-radical oxidation pathway lies in its selectivity, enabling it to selectively degrade electron-rich organic pollutants.[13] The non-radical oxidation pathway exhibits significant resistance to common organic matter and inorganic anions and does not produce halogenated disinfection by-products during the oxidation process.[14] Non-radical oxidation pathways could selectively degrade electron-rich pollutants and are resistant to conventional radical quenchers.[15] However, due to the low mineralization capacity of non-radical oxidation pathways, the reaction mechanisms and influencing factors in actual soil and groundwater remediation remain unclear.

Furthermore, the degradation behaviors of structurally similar TBBPA and TBBPS under non-radical oxidation pathways are not well defined.

Catalysts play a critical role in the activation of persulfate and the formation of non-radical oxidation pathways. The synthesis temperature, crystal structure, defects and particle size of the catalysts could effectively modulate the activation pathway of PS-AOPs.[16–18] For instance, Fe–N/C catalysts synthesized at lower temperature (300 °C) activate PMS to generate electron transfer processes, while those synthesized at higher temperatures (>700 °C) facilitate the production of $^1O_2$ and high-valent iron active species.[19] Amorphous $Ni(OH)_2$ with an electron-rich active surface promotes free radical oxidation pathways, while crystalline $Ni(OH)_2$ is more favorable for non-radical oxidation pathways.[20] The introduction of sulfur vacancies in chalcopyrite ($FeCuS_2$) has been shown to shift PMS activation from free radicals to $^1O_2$.[21] The size of Cu particles affects their catalytic performance, with Cu sub-nanoparticles exhibiting electrophilic properties and favoring the non-radical oxidation pathways, while larger Cu nanoclusters are nucleophilic and promote radical oxidation pathways.[22] Metal doping has a significant effect on regulating non-radical oxidation pathways. Bimetal co-doped catalysts have gained attention due to their flexible atom selection, superior synergistic effect, and tunability in promoting non-radical oxidation pathways.[23] Sulfurized carbon nitride has been proved to have higher catalytic activity for persulfate than carbon nitride,[24] and S doping can improve the metal loading on the support.[25] Therefore, sulfurized carbon nitride was selected as the support.

Inspired by the above, recyclable Fe and Cu co-doped sulfurized carbon nitride catalysts (FeCuS@GFs) were designed for the effective removal of TBBPA/S from soil and groundwater. Quenching experiments, chemical probes, and electron paramagnetic resonance (EPR) tests demonstrated that FeCuS@GFs can activate PDS and PMS to produce electron transfer processes and high-valent metal active species, respectively. Comparative studies revealed that high-valent metal active species in the FeCuS@GFs/PMS system exhibited higher oxidative capacity than the electron transfer process in the FeCuS@GFs/PDS system. Comprehensive experimental analyses and theoretical calculations demonstrated that TBBPA is more susceptible to degradation by non-radical oxidation pathways than TBBPS, and revealed the intrinsic molecular mechanism. The application of FeCuS@GFs/persulfate systems in actual soils reveals the effect of soil physicochemical properties on the non-radical oxidation pathways. This work advances the understanding of non-radical oxidation pathways in PS-AOPs and provides valuable insights into their application for the removal of POPs from soil and groundwater.

2. Materials and methods

2.1 Chemicals and soil samples

Comprehensive details regarding the chemicals used are provided in Text S1.

Eight representative soil samples (0–20 cm depth) were collected from various provinces across China, including Heilongjiang (HLG), Jiangsu (JS), Jiangxi (JX), Shandong (SD), Guangdong (GD), Ningxia (NX), Sichuang (SC), and Chongqing (CQ). Detailed information of soil samples is provided in Table S1. The physical and chemical properties of these soils cover most soils in China. Following air drying, large particles and plant roots were removed, and the soil samples were ground and sieved through a 1 mm mesh to obtain clean soil. 1000 g of clean soil was spiked with TBBPA and TBBPS to achieve the target concentration of 200 mg kg^{-1} and then aged in a dark and ventilated environment for two weeks. Detailed information about the spiking process is shown in Text S2.

2.2 Synthesis and characterization of FeCuS@GFs

$Fe(NO_3)_3{\cdot}9H_2O$ (1 mmol), $Cu(NO_3)_2{\cdot}3H_2O$ (1 mmol) and L-cysteine (0.5, 1.0, 2.0, 3.0 g) were dissolved in ultrapure water (40 mL). After stirring at 60 °C for 1 h, urea (20 g) was added to the mixture with continued stirring until completely dissolved. Graphite felt (GF) was soaked in 0.1 M HCl for 12 h and then washed repeatedly with ultrapure water until the washing water was neutral. After drying, the washed GF was cut into 1 cm × 1 cm pieces. 1 mL of mixture was dripped onto one GF piece, then the treated GF piece was dried at 60 °C. Dried GF pieces were put in a crucible wrapped with aluminum foil to reduce gas leakage. The crucibles were heated at 550 °C for 2 h at a heating rate of 5 °C min^{-1}. After cooling to room temperature, the material was collected, washed with 0.1 M HCl and ultrapure water, and then dried at 70 °C. According to the amounts of L-cysteine, the obtained

materials were denoted as FeCuS@GF-0.5, FeCuS@GF-1.0, FeCuS@GF-2.0, and FeCuS@GF-3.0. The average weight of each piece is 0.624 ± 0.113 g. The characterization methods of FeCuS@GFs are presented in Text S3.

2.3 Experimental procedures

The catalytic performance of FeCuS@GFs was investigated by batch experiments on the degradation of TBBPA and TBBPS. The effect of solution pH and PDS/PMS dosage on TBBPA/S degradation was investigated. Quenching and chemical probe experiments were conducted to identify the active species. The removal efficiency of TBBPA/S in the different kinds of soils was investigated in the FeCuS@GFs/PDS and FeCuS@GFs/PMS systems. Detailed experimental methods are presented in Text S4. Since the FeCuS@GFs are in bulk form, they can be easily separated after slurry experiments.

2.4 Analytical methods

The concentrations of TBBPA, TBBPS, PMSO and $PMSO_2$ were analyzed using a high-performance liquid chromatography (HPLC) instrument with a diode array detector (LC-20A, SHIMADZU) equipped with a C18 column (250 mm × 4.6 mm, 5 μm particle, Agilent). The mobile phases and detection wavelengths are shown in Table S2. Detailed information about the extraction methods for TBBPA/S in soil, EPR spectrometer, and electrochemical measurements is provided in Text S5. The octanol–water partition coefficients ($\log K_{ow}$) of target compounds were predicted by the quantitative structure–activity relationship (QSAR)-based EPI Suite software.

3. Results and discussion

3.1 Characterization of FeCuS@GFs

The morphology and elemental distribution of FeCuS@GF-2.0 were observed using scanning electron microscopy (SEM) and transmission electron microscopy with energy-dispersive X-ray spectroscopy (TEM-EDS). As shown in Fig. 1 and S1, FeCuS@GF-2.0 was a bulk material formed by FeCuS and graphite fibers, and FeCuS with a mushroom shape grows on the surface of the graphite fibers. Ultrasound-assisted detachment and subsequent TEM imaging (Fig. 1c) revealed that FeCuS has a layered structure with a small number of pores and a particle size of ~856 nm, while no distinct metal nanoparticles were observed, indicating that Fe and Cu atoms might be atomically dispersed on the support.[26] As shown in the high-angle annular dark-field scanning transmission electron microscopy (HAADF-STEM) image (Fig. 1d), exceptionally bright light dots represent metal atoms on the support, indicating that Fe and Cu might dope on the support successfully. The uniform distribution of Fe and Cu atoms was also validated by EDS mapping (Fig. 1e–i). The X-ray diffraction (XRD) spectra show two wide diffraction peaks at 26° and 44° observed in as-prepared FeCuS@GFs (Fig. S2a), which was a typical signal of sulfurized carbon nitride.[27] In addition, the absence of metal phase diffraction peaks in XRD further indicated that Fe and Cu might be highly dispersed,[28] consistent with HAADF-STEM images.

Fourier-transform infrared (FTIR) spectra (Fig. S2b) identified key functional groups in FeCuS@GFs, including tri-*s*-triazine ring vibration (810 cm^{-1}), aromatic sp^3C–N and sp^2-C=N stretching vibrations (1250–1630 cm^{-1}), and C≡N vibration (2176 cm^{-1}),[29,30] suggesting that FeCuS@GFs had the structure of carbon nitride. These signals were significantly

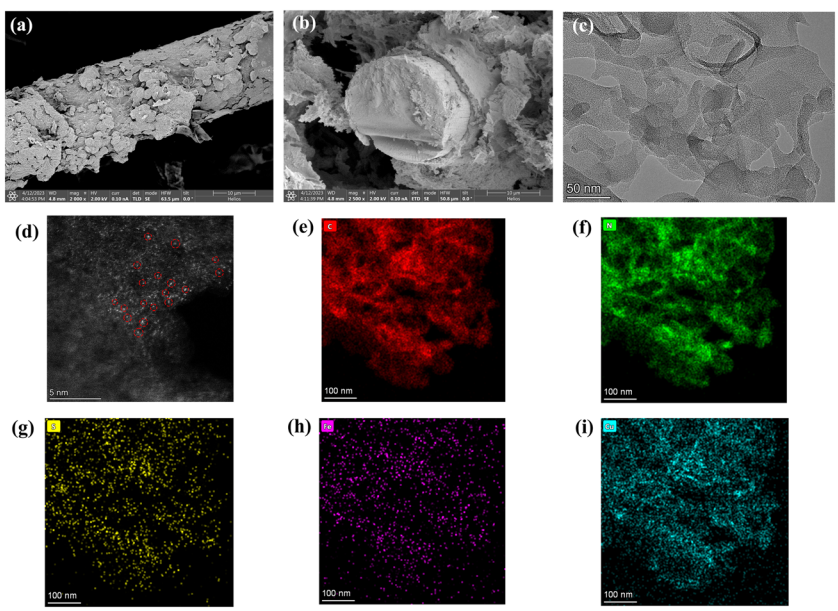

Fig. 1 (a and b) SEM, (c) TEM, (d) HAADF-STEM, and (e–i) EDS mapping of FeCuS@GF-2.0.

reduced with increasing L-cysteine addition during synthesis, suggesting the competitive relationship between N and S doping.[31] According to the adsorption/desorption isotherm curves of as-prepared FeCuS@GFs (Fig. S2c), the specific surface areas of FeCuS@GF-0.5, FeCuS@GF-1.0, FeCuS@GF-2.0, and FeCuS@GF-3.0 were 13.93, 16.47, 12.76, and 18.56 $m^2\ g^{-1}$, respectively, and the pore volumes were 0.070, 0.098, 0.063, and 0.097 $cm^3\ g^{-1}$, respectively, suggesting that the addition of L-cysteine had minimal impact on the specific surface area and pore volume of FeCuS@GFs. The graphitization degree of the carbon materials can be characterized by Raman spectra. As shown in Fig. S2d, the I_D/I_G value (Raman D band-to-G band intensity ratio) of FeCuS@GF-2.0 was 1.10, higher than that of FeCuS@GF-0.5 (I_D/I_G = 1.06), FeCuS@GF-1.0 (I_D/I_G = 1.05), and FeCuS@GF-3.0 (I_D/I_G = 1.07), suggesting that FeCuS@GF-2.0 possessed more defects, which can enhance the electron delivery of the materials.[32]

The elemental composition and valence state of FeCuS@GFs were characterized by X-ray photoelectron spectroscopy (XPS). As summarized in Table S3, all FeCuS@GFs contained C, N, O, S, Fe, and Cu elements, and the content of Fe and Cu in different FeCuS@GFs had no significant difference, with values of ~0.4% and ~0.5%, respectively. According to the results of ICP-MS (Table S3), the Fe loadings of FeCuS@GF-0.5, FeCuS@GF-1.0, FeCuS@GF-2.0, and FeCuS@GF-3.0 were 3.12, 2.92, 2.92, and 3.05 wt%, and the corresponding Cu loadings were 3.61, 3.52, 3.45, and 3.45 wt%, respectively. This resulted in Fe/Cu molar ratios of 0.99, 0.95, 0.97, and 1.01. With the increasing of L-cysteine addition (from 0.5 to 3.0 g), the S content increased from 0.22% to 0.42%, and the C content increased from 45.11% to 57.51%, while the N content decreased from 49.13% to 37.61%, further supporting the N-to-S substitution effect.[33] As shown in Fig. 2a, the peaks with binding energies of 284.8, 287.9, and 288.3 eV in the high-resolution C 1s spectrum belonged to C–C, C–O, and C–N, respectively.[34] The high-resolution N 1s spectrum of FeCuS@GF-2.0 was deconvoluted into four peaks at 398.3, 399.0, 400.0, and 401.0 eV, which were ascribed to pyridinic N, N-metal, pyrrolic N, and graphitic N,[35,36] respectively (Fig. 2b). These N-, O-, or S-containing functional groups had been demonstrated to be effective active sites for persulfate activation.[37,38] The Fe $2p_{3/2}$ and Fe $2p_{1/2}$ energy was 710.3 and 723.1 eV (Fig. 2e), respectively, suggesting that the Fe of FeCuS@GF-2.0 was predominantly in the form of Fe(III).[39] The high-resolution XPS spectra of Cu 2p can be partitioned into Cu(I) and Cu(II) (Fig. 2f). Peaks at 932.8 and 952.4 eV were generated by Cu(I), while peaks at 935.5 and 955.2 eV with distinct satellite peaks (944.4 eV) originated from Cu(II).[40] Fe and Cu in different valence states may act as active sites in a synergistic manner to enhance their activation of persulfate.[41,42] Notably, FeCuS@GF-2.0 had the highest Cu(I) content (74.11%) among all the FeCuS@GFs (Fig. 2 and S3–S5).

3.2 Catalytic performance evaluation of FeCuS@GFs

3.2.1 Performance of different FeCuS@GFs. The catalytic performance of FeCuS@GFs was assessed through the removal of TBBPA/S in PDS and PMS systems. As shown in Fig. 3, GF had no catalytic activity on persulfate, but FeS@GF, CuS@GF and all FeCuS@GFs can activate PDS and PMS for TBBPA/S removal. Notably, the catalytic activity of FeCuS@GFs was greater than that of FeS@GF and CuS@GF, suggesting that the co-doping of Fe and Cu could significantly enhance the activity to persulfate. The removal efficiency of TBBPA with different FeCuS@GFs showed no significant differences in both PDS and PMS systems (Fig. 3a and b), suggesting that the active species generated in both systems could oxidize TBBPA efficiently. However, significant differences in TBBPS removal efficiency were observed, as shown in Fig. 3c and d. In the PDS system, FeCuS@GF-2.0 exhibited the highest TBBPS removal efficiency (76.8%), while in the PMS system, TBBPS was almost removed with FeCuS@GF-2.0 and FeCuS@GF-3.0 (Fig. 3d). These results demonstrated that TBBPS was more difficult to remove than TBBPA in both PDS and PMS systems and that FeCuS@GF-2.0

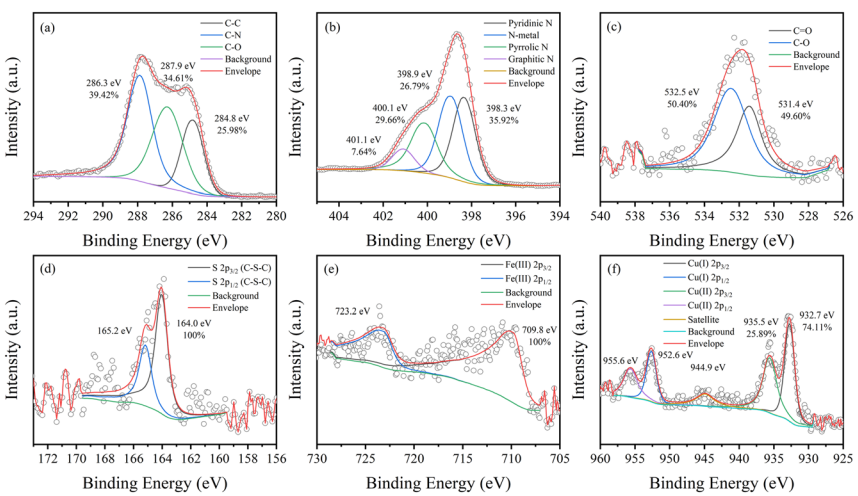

Fig. 2 The high-resolution (a) C 1s, (b) N 1s, (c) O 1s, (d) S 2p, (e) Fe 2p, and (f) Cu 2p XPS spectra of FeCuS@GF-2.0.

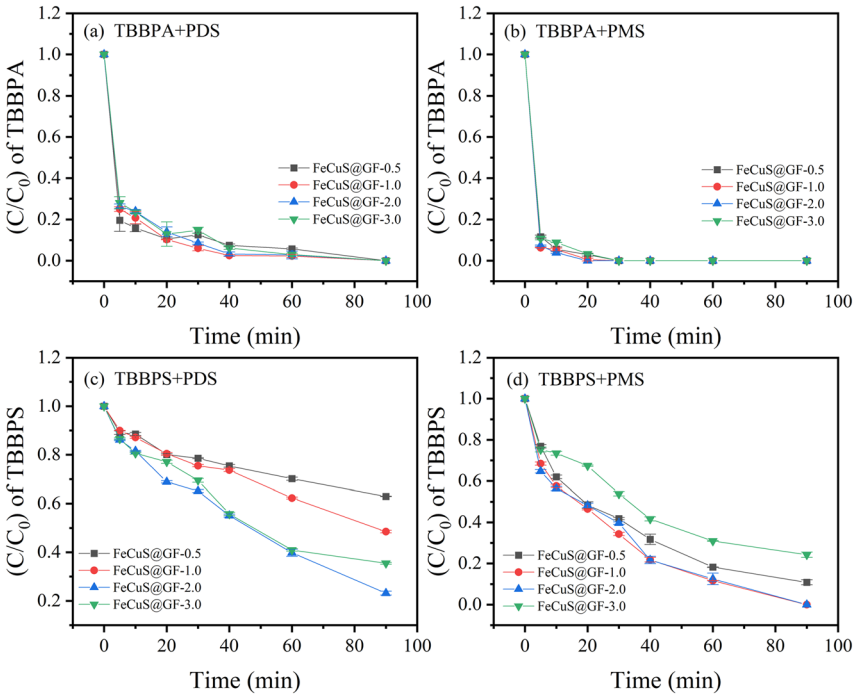

Fig. 3 The removal efficiency of (a and b) TBBPA and (c and d) TBBPS in different FeCuS@GFs/PDS or FeCuS@GFs/PMS systems. Experimental conditions: [PDS] = 0.5 mM, [PMS] = 0.1 mM, [TBBPA] = [TBBPS] = 2 mg L^{-1}, pH = 5.6.

exhibits superior catalytic performance for persulfate activation to remove TBBPA/S. Consequently, FeCuS@GF-2.0 was selected as the catalyst for subsequent experiments. FeCuS@GF-2.0 with the highest I_D/I_G value (1.10) and Cu(I) content (74.11%) exhibited better catalytic activity, indicating that performance variations might stem from structural defects and Cu(I) species. Additionally, complete removal of TBBPA was achieved in the FeCuS@GF-2.0/PDS system within 90 min (Fig. 3a), while the FeCuS@GF-2.0/PMS system achieved the same result in just 30 min (Fig. 3b). TBBPS was removed more rapidly in the FeCuS@GF-2.0/PMS system than in the FeCuS@GF-2.0/PDS system (Fig. 3c and d). These findings suggest that the active species generated in the FeCuS@GF-2.0/PMS system were more effective in removing TBBPA/S compared to those in the FeCuS@GF-2.0/PDS system.

3.2.2 Effect of PDS or PMS dosages. The influence of PDS and PMS concentrations on the removal efficiency of TBBPA and TBBPS in the FeCuS@GF-2.0 system was systematically evaluated (Fig. S6). In the absence of PDS or PMS (0 mM), FeCuS@GF-2.0 could adsorb ~60% of TBBPA or ~10% of TBBPS. This discrepancy is potentially due to the higher octanol–water partition coefficient of TBBPA ($\log K_{ow}$ = 7.20) compared to TBBPS ($\log K_{ow}$ = 5.21). The concentration of TBBPA/S adsorbed on the FeCuS@GF-2.0 was investigated after the end of the reaction (90 min). As shown in Fig. S7, the adsorption of TBBPA/S reached 101.0 mg kg^{-1} when the dosage of persulfate was 0 mM. However, upon the addition of persulfate, the adsorption of TBBPA/S on FeCuS@GF-2.0 was below 10 mg kg^{-1} and decreased with the increase of persulfate dosage, suggesting that the adsorption of TBBPA/S on FeCuS@GF-2.0 was not negligible.

As shown in Fig. S6a and b, the addition of only 0.1 mM PDS or 0.01 mM PMS could remove ~40% of TBBPA, and the increasing of PDS or PMS concentration can enhance its removal efficiency. For TBBPS, the degradation efficiency increased progressively (from 38.5% to 71.1%) with increasing PDS dosage (from 0.1 to 0.5 mM). However, further increases in PDS concentration (from 0.5 to 1.0 mM) had little additional effect (Fig. S6c). This suggested that the PDS concentration had a positive but limited effect on TBBPS degradation, likely due to the saturation of active sites available in FeCuS@GF-2.0. In contrast, Fig. S6d demonstrated that TBBPS degradation efficiency increased from 36.1% to 100% as PMS dosage rose from 0.01 to 0.5 mM. The reason why PMS did not encounter the limitation of saturation of active sites is given in Text S6. These results indicated that the active species produced in the two systems were different, with the active species in the PMS system exhibiting higher activity.

As depicted in Fig. S8, when the concentration of PDS and PMS was 0.1 mM, distinct kinetic profiles were observed for persulfate consumption between the two systems. The consumption of persulfate in the TBBPA system was significantly greater than that in the TBBPS system, indicating that TBBPA was more susceptible to oxidation than TBBPS. Furthermore, the consumption of PMS exceeded that of PDS in both systems, suggesting that the active species derived from PMS may possess greater reactivity compared to those generated from PDS.

3.2.3 Effect of the solution pH. The solution pH plays a crucial role in the degradation of TBBPA and TBBPS, so the effect of initial solution pH on the FeCuS@GF-2.0/PDS and

FeCuS@GF-2.0/PMS systems was investigated. As shown in Fig. S9a, in the FeCuS@GF-2.0/PDS system, the removal efficiency of TBBPA decreased gradually as the pH increased, with almost no removal observed at pH 11.0. This trend is likely due to the electrostatic repulsion between negatively charged TBBPA (predominantly in its deprotonated form, $TBBPA^{2-}$, at pH >8.5) and PDS ($S_2O_8^{2-}$), which inhibits adsorption and reaction.[43] Additionally, the zeta potential of FeCuS@GF-2.0 decreased from 6.4 to −43.5 mV with increasing pH (Fig. S10), further reducing interactions between catalyst and TBBPA. A similar trend was observed for TBBPS, with negligible removal at pH 11.0 in both systems (Fig. S9c and d). However, the removal efficiency of TBBPA in the FeCuS@GF-2.0/PMS system did not significantly decline over the pH range of 3.0–11.0 (Fig. S9b), suggesting that electrostatic repulsion did not significantly impact the reaction in this system, which might be due to the active species produced in the PMS system being more active. The effect of pH on the catalytic process mainly involved different reaction mechanisms in the PDS or PMS system, and detailed discussion is presented in Text S7. The difference in TBBPA/S removal efficiency between the two systems revealed that TBBPS was more difficult to remove than TBBPA and that the active species in the FeCuS@GF-2.0/PMS system exhibited higher activity than those in the FeCuS@GF-2.0/PDS system. The dissolution of metal species (Fe and Cu) from FeCuS@GF-2.0 and the contribution of leached solution to degradation were investigated (Fig. S11 and S12). Before the reaction, the dissolution of Fe and Cu from FeCuS@GF-2.0 increased with decreasing pH, and the concentrations of Fe and Cu were in the range of 0.51–0.66 mg L^{-1} (Fig. S11). After the reaction, the concentrations of leached Fe and Cu increased, and the highest values were observed at pH 3.0 with 2.3 and 0.96 mg L^{-1} in the TBBPA and PMS system (Fig. S11b), respectively. The leaching of Fe and Cu was monitored during the cyclic use of FeCuS@GF-2.0 at pH 3.0. As shown in Fig. S13, the leached metal concentration gradually decreased with the cyclic use of FeCuS@GF-2.0 and was significantly lower than that specified by the National Primary Drinking Water Regulations in the USA (Cu <1.3 mg L^{-1}) and Environmental Quality Standards for Surface Water (GB 3838-2002) in China (Cu <1.0 mg L^{-1}). As shown in Fig. S12, the leached Fe and Cu could activate persulfate to degrade TBBPA/S, but the degradation efficiency was below 50%, suggesting that the degradation of TBBPA/S is dominated by heterogeneous catalysis. As shown in Fig. S13 and S23, the leached metal concentration gradually decreased with the cyclic use of FeCuS@GF-2.0 in the PMS system, but the degradation efficiency of TBBPA remained above 95%, suggesting that the contribution of homogeneous catalysis was negligible.

3.3 Identification of active species

3.3.1 Quenching experiments and EPR analysis. Various scavengers were used to selectively quench reactive species. Ethanol (EtOH) was employed to quench both sulfate radicals ($SO_4^{\cdot-}$) and hydroxyl radicals (·OH), whereas *tert*-butanol (TBA) was used as a selective scavenger for ·OH.[44,45] Furfuryl alcohol (FFA) and dimethyl sulfoxide (DMSO) were used as scavengers for $^1O_2$ and high-valent metal active species, respectively.[39,46,47] The degradation efficiency of TBBPA and TBBPS in the FeCuS@GF-2.0/PDS system was not significantly changed with the addition of EtOH, TBA, FFA and DMSO (Fig. 4a and b), suggesting that neither $SO_4^{\cdot-}$, ·OH, $^1O_2$, nor high-valent metal active species played a major role. To further identify the presence of $SO_4^{\cdot-}$, ·OH and $^1O_2$, 5,5-dimethyl-1-pyrroline *N*-oxide (DMPO) and 2,2,6,6-tetramethyl-4-piperidinol (TEMP) were used to obtain the EPR spectra of the FeCuS@GF-2.0/PDS system. No signals corresponding to DMPO–SO_4, DMPO–OH, or TEMPO were detected (Fig. 4c and d), suggesting that $SO_4^{\cdot-}$, ·OH and $^1O_2$ were absent in the FeCuS@GF-2.0/PDS system.

As shown in Fig. 5a and b, the addition of EtOH and TBA slightly inhibited the TBBPA and TBBPS removal in the FeCuS@GF-2.0/PMS system, suggesting $SO_4^{\cdot-}$ and ·OH made limited contributions. The weak signals of DMPO–OH observed in the EPR spectra of the FeCuS@GF-2.0/PMS system (Fig. 5c) confirmed the presence of small amounts of ·OH in the reaction system. Additionally, in the FeCuS@GF-2.0/PMS system, a distinct signal of DMPOX and TEMPO was observed in the EPR spectra (Fig. 5d),[48,49] suggesting the possible presence of $^1O_2$. However, the addition of FFA did not significantly inhibit the degradation of TBBPA/S. These results of EPR spectra and quenching experiments suggested the presence of additional active species capable of degrading TBBPA/S in the FeCuS@GF-2.0/PMS system. Notably, the addition of 100 mM DMSO resulted in a reduction in TBBPA and TBBPS removal. As shown in Fig. S14, the reduction of TBBPA/S removal increased with the concentration of DMSO increasing from 100 mM to 600 mM, suggesting that high-valent metal active species might be the dominant active species in the FeCuS@GF-2.0/PMS system.

3.3.2 Electrochemical and probe experiments. To further determine the presence of the electron transfer process, electrochemical analyses were carried out in the two systems. As shown in the linear sweep voltammetry (LSV) curves (Fig. 6b), the current on the FeCuS@GF-2.0 electrode increased significantly after adding PDS and TBBPS to the reaction solution, indicating that an electron transfer process occurred when both PDS and TBBPS were added into the reaction solution.[50] However, no increase of current at the FeCuS@GF-2.0 electrode was observed in the FeCuS@GF-2.0/PMS system (Fig. 6c), indicating that an electron transfer process did not occur in this system. Open-circuit potential (OCP) curves of the FeCuS@GF-2.0 electrode further reflected this current response. The potential of the FeCuS@GF-2.0 electrode increased after adding PDS, then the potential dropped instantaneously with the addition of TBBPS (Fig. 6d). With the addition of TBBPS, electrons were transferred from TBBPS (electron donor) to PDS (electron acceptor) *via* the FeCuS@GF-2.0 surface, resulting in a

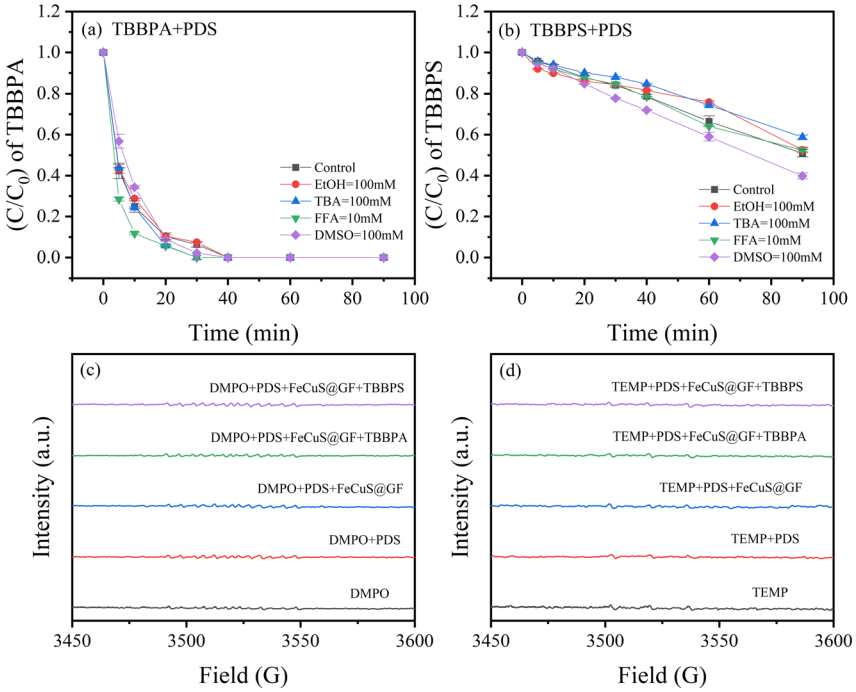

Fig. 4 The effect of EtOH, TBA, FFA and DMSO on the TBBPA (a) and TBBPS (b) degradation and EPR spectra obtained by spin trapping with DMPO (c) and TEMP (d) in the FeCuS@GF-2.0/PDS system. Experimental conditions: [PDS] = 0.5 mM, [TBBPA] = [TBBPS] = 2 mg L^{-1}, pH = 5.6.

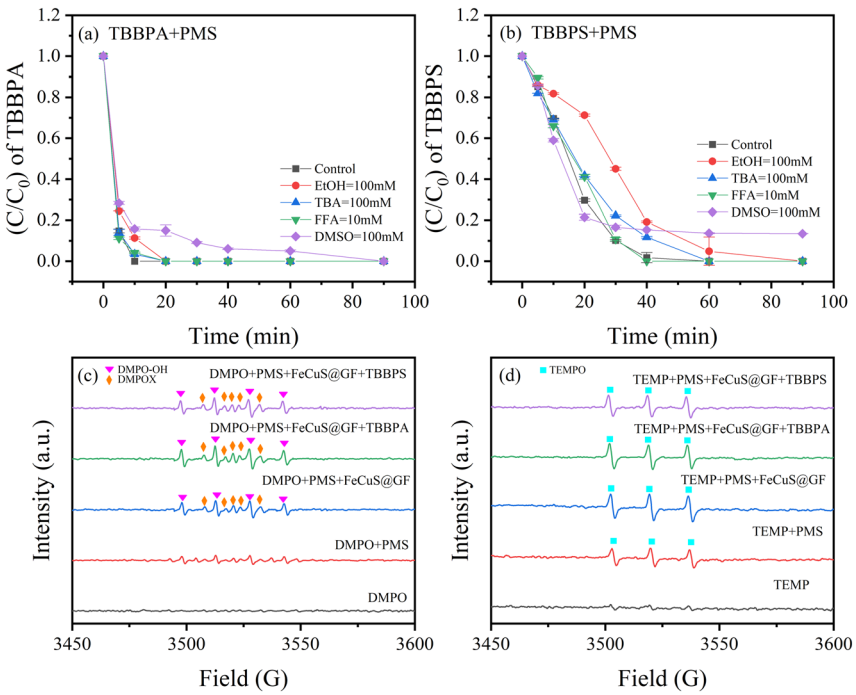

Fig. 5 The effect of EtOH, TBA, FFA and DMSO on the TBBPA (a) and TBBPS (b) degradation and EPR spectra obtained by spin trapping with DMPO (c) and TEMP (d) in the FeCuS@GF-2.0/PMS system. Experimental conditions: [PMS] = 0.1 mM, [TBBPA] = [TBBPS] = 2 mg L^{-1}, pH = 5.6.

decrease in its potential,[51,52] demonstrating that FeCuS@GF-2.0 could act as an electron shuttle to facilitate electron transfer. In contrast, the potential of the FeCuS@GF-2.0 electrode decreased slightly with the addition of TBBPS only, implying that the electron transfer process occurred only in the FeCuS@GF-2.0/PDS system. The electron transfer efficiency of the as-prepared catalysts was investigated by electrochemical impedance spectroscopy (EIS). As shown in

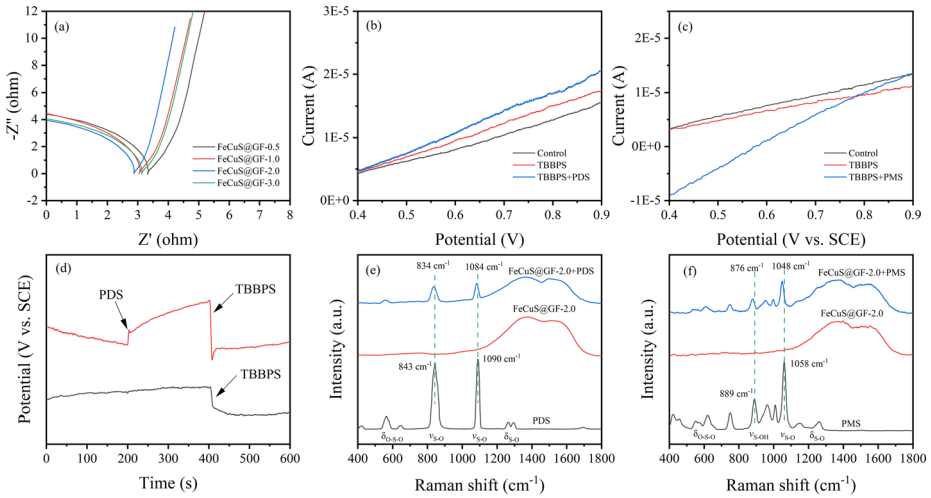

Fig. 6 (a) EIS curves of different FeCuS@GFs. LSV curves of FeCuS@GF-2.0 electrodes in the (b) FeCuS@GF-2.0/PDS and (c) FeCuS@GF-2.0/PMS systems. (d) Open-circuit potential curves of the FeCuS@GF-2.0 electrodes in different systems. *In situ* Raman spectra of (e) FeCuS@GF-2.0/PDS and (f) FeCuS@GF-2.0/PMS systems.

Fig. 6a, FeCuS@GF-2.0 had a smaller semicircle diameter than the other catalysts, suggesting that the electron transfer resistance of FeCuS@GF-2.0 was lower than that of the other catalysts. These results suggested that the electron transfer process was the main pathway for degrading pollutants in the FeCuS@GF-2.0/PDS system.

To determine the type of high-valent metal active species (Fe(IV) or Cu(III)), methyl phenyl sulfoxide (PMSO) probe experiments were conducted (Fig. S15). PMSO can be selectively oxidized to methyl phenyl sulfone ($PMSO_2$) by Fe(IV), but PMSO exhibits no reactivity toward Cu(III).[53] In the PDS alone and FeCuS@GF-2.0/PDS systems, PMSO oxidation was negligible, and $PMSO_2$ formation was minimal (Fig. S15a and b), suggesting the absence of Fe(IV) in the FeCuS@GF-2.0/PDS system. However, the oxidation of PMSO and the production of $PMSO_2$ were clearly observed in the FeCuS@GF-2.0/PMS system (Fig. S15c and d). 60.5% of PMSO was oxidized and 51.0% of $PMSO_2$ was produced in the FeCuS@GF-2.0/PMS system, while the oxidation efficiency of PMSO and the production efficiency of $PMSO_2$ were only 25.5% and 26.8% in the PMS alone system. These results showed that Fe(IV) was the primary active species in the FeCuS@GF-2.0/PMS system. Consequently, the observed conversion of PMSO to $PMSO_2$ (Fig. S15) provided evidence for the generation of Fe(IV) in PMS systems. The redox potential of the Fe(IV)/Fe(III) couple is 2.00 V[54] compared to 1.57 V for the Cu(III)/Cu(II) couple.[55] This thermodynamic disparity favours the reaction between Fe(IV) and Cu(II), resulting in the production of small amounts of Cu(III). However, Cu(III) undergoes rapid decomposition under acidic conditions,[56,57] yielding ·OH.[58] In addition, the oxidation of PMSO was higher than the production of $PMSO_2$ (60.5% *vs.* 51.0%), which showed that ~9.5% of PMSO was removed instead of producing $PMSO_2$, suggesting that minor amounts of free radicals and Cu(III) may also be present in the FeCuS@GF-2.0/PMS system. Thus, although Fe(IV), Cu(III), and ·OH might coexist within the system, Fe(IV) constituted the primary active species.

3.3.3 Surface adsorption and activation of PDS and PMS. The adsorption and activation behavior of PDS and PMS on the FeCuS@GF-2.0 surface was investigated using *in situ* Raman spectroscopy. As shown in the Raman spectrum of PDS (Fig. 6e), the peaks at 500–650 cm^{-1} and 1200–1400 cm^{-1} belonged to O–S–O deformation (δ_{O-S-O}) and S–O deformation (δ_{S-O}), and the peaks at 843 and 1090 cm^{-1} were attributed to S–O symmetric vibration (ν_{S-O}).[59,60] After dropping PDS solution onto the FeCuS@GF-2.0 surface, the peak of ν_{S-O} became wider and shifted from 843 and 1090 cm^{-1} to 834 and 1084 cm^{-1}, suggesting that PDS was combined with FeCuS@GF-2.0 to produce a $S_2O_8^{2-}$* complex.[61] These results indicated that PDS would combine onto the surface of FeCuS@GF-2.0 to form the $S_2O_8^{2-}$* complex, which could be consumed *via* the electron transfer process. As shown in the Raman spectrum of PMS (Fig. 6e), the peaks of δ_{O-S-O}, δ_{S-O}, ν_{S-O} and S–OH symmetric vibration (ν_{S-OH}) were observed at 500–650, 1200–1400, 1058 and 889 cm^{-1}, respectively. Compared with the original spectrum of PMS, the peaks of ν_{S-O} and ν_{S-OH} shifted to 1048 and 876 cm^{-1}, suggesting that PMS interacted with FeCuS@GF-2.0 strongly to produce a HSO_5^-* complex.[62] Notably, the shifting of ν_{S-O} and ν_{S-OH} in the FeCuS@GF-2.0/PMS system (6 and 9 cm^{-1}) was much higher than that in the FeCuS@GF-2.0/PDS system (10 and 13 cm^{-1}), suggesting that HSO_5^-* was more active than $S_2O_8^{2-}$*. In summary, the oxidation of TBBPA/S was mainly through an electron transfer oxidation pathway in the FeCuS@GF-2.0/PDS system, while TBBPA/S was oxidized by Fe(IV) active species as the main active species in the FeCuS@GF-2.0/PDS system.

3.4 Reaction mechanism

3.4.1 Catalytic centers of FeCuS@GF-2.0. To identify the active catalytic centers responsible for persulfate activation, used FeCuS@GF-2.0 was characterized by XRD, FTIR, and XPS. FeCuS@GF-2.0 that has been used once and continuously 5

times was referred to as 1st-FeCuS@GF-2.0 and 5th-FeCuS@GF-2.0, respectively. As shown in Fig. S16a, no significant shifts in diffraction peaks of the used FeCuS@GF-2.0 were observed in both PDS and PMS systems as the frequency of use increased, suggesting that the crystal structure of FeCuS@GF-2.0 is relatively stable. In the FTIR spectra (Fig. S16b), the signal of C≡N (2176 cm^{-1}) and the tri-*s*-triazine structure (810 cm^{-1}) became weaker as the number of uses increased, indicating that C≡N and tri-*s*-triazine functional groups might be progressively oxidized. In addition, the signal of C≡N and tri-*s*-triazine functional groups of 5th-FeCuS@GF-2.0-PMS was weaker than those of 5th-FeCuS@GF-2.0-PDS, suggesting the produced active species in the PMS system had stronger oxidation ability, which is more destructive to the structure of FeCuS@GF-2.0. This was consistent with the finding that the degradation efficiency of TBBPA/S in the FeCuS@GF-2.0/PMS system was significantly higher than that in the FeCuS@GF-2.0/PDS system.

As shown in Fig. 3, the activation of the catalysts for persulfate increased with the addition of L-cysteine increasing, which suggested that the S-containing functional groups may be the main active sites. The surface S content of the used FeCuS@GF-2.0 remained relatively stable after multiple reaction cycles (Table S3). However, as presented in the high-resolution XPS of S 2p (Fig. S17d–S20d), the thiophene S in the FeCuS@GF-2.0 gradually converted into oxidized S after 5 consecutive uses, suggesting that thiophene S may be the main active site.[63] The O content of used FeCuS@GF-2.0 increased with the number of uses (Table S3), indicating that FeCuS@GF-2.0 was oxidized during the reaction. As shown in the high-resolution XPS of O 1s (Fig. S17c–S20c), the C=O contents of 1st-FeCuS@GF-2.0-PDS and 5th-FeCuS@GF-2.0-PDS were 53.48% and 56.43%, respectively, while those of 1st-FeCuS@GF-2.0-PMS and 5th-FeCuS@GF-2.0-PMS were 60.84% and 43.17%, respectively, which suggested that C=O was the main active site for PMS but not for PDS.[64,65] Notably, the proportion of Cu(I) of used FeCuS@GF-2.0 decreased (Table S4) in both systems, but the total Cu content did not change significantly (Table S3). In the PMS system, the total Cu contents of FeCuS@GF-2.0, 1st-FeCuS@GF-2.0 and 5th-FeCuS@GF-2.0 were 0.53%, 0.57% and 0.59%, respectively, but the corresponding proportions of Cu(I) were 74.11%, 39.72% and 41.53%, respectively. The same phenomenon was observed in the PDS system, indicating that Cu(I) might be the main active site for PDS and PMS.[66,67] In addition, the contents of pyrrolic N had significantly decreased (Table S3). For example, the contents of pyrrolic N of FeCuS@GF-2.0, 1st-FeCuS@GF-2.0-PMS, and 5th-FeCuS@GF-2.0-PMS were 29.66%, 17.71%, and 16.32%, respectively, suggesting that pyrrolic N might be the main active species.[68] Based on these findings, the active sites of FeCuS@GF-2.0 may be thiophene S, C=O, Cu(I), and pyrrolic N.

3.4.2 DFT calculation of TBBPA/S reaction sites. DFT calculation is a very useful method to predict the electrophilic reactivity and reaction sites of pollutants. The Fukui function[69] and dual descriptor[70] were widely used to identify the reaction sites. Theoretically, sites with higher values of Fukui function (f^+, f^- and f^0) correspond to higher activities of nucleophilic, electrophilic, and free reactions, respectively.[71] Sites with larger negative values of the dual descriptor are more susceptible to electrophilic reactions, while sites with larger positive values are more susceptible to nucleophilic attack. Atoms of TBBPA/S molecules with relatively high f^- and relatively negative dual descriptor values are marked in orange (Tables S5 and S6), and the f^- and dual descriptor equivalent surface is presented in Fig. S21. 5O and 6O of TBBPA exhibited the largest f^- values and the most negative dual descriptor values, suggesting that 5O and 6O may be the reaction sites of electrophilic attack. The f^- values of 21Br, 24Br, 17O and 19O in TBBPS were 0.0866, 0.0866, 0.0688, and 0.0688, higher than that of other atoms, and relatively negative dual descriptor values were also exhibited by 21Br, 24Br, 17O and 19O, implying that 21Br, 24Br, 17O and 19O may be the reaction sites of TBBPS.

Electrostatic potential surface (EPS) is a way of describing the charge distribution on the surface of a molecule, reflecting the electrostatic influence of charges at different locations, which helps to understand how molecules interact with other molecules.[72] As shown in Fig. S22a, due to the dense electron cloud of lone pair electrons of the hydroxyl oxygen atom, the minimum position of EPS on the TBBPA surface was near the hydroxyl oxygen atom, with an electrostatic potential value of −41.11 and −41.09 kcal mol^{-1}, further suggesting that the hydroxyl of TBBPA served as the primary reaction site. The minimum region of EPS on the TBBPS surface was near the sulfone oxygen atom (−56.38 and −54.51 kcal mol^{-1}) and the hydroxyl oxygen atom (−24.61 and −24.57 kcal mol^{-1}) (Fig. S22b). Considering the Fukui function and dual descriptor results of TBBPS, the hydroxyl groups in TBBPS were hypothesized to be the main reaction sites. Compared with the electrostatic potential values of the region near the hydroxyl oxygen atom in TBBPA and TBBPS, it could be found that the electrophilic reactivity of TBBPA is higher than that TBBPS, corresponding to the results shown in Fig. 3. The EPS results for TBBPA/S indicated that the electrophilic potential at the hydroxyl group of TBBPA is lower than that of TBBPS, suggesting that TBBPA is more susceptible to electrophilic reactions than TBBPS.[73] This is consistent with the results shown in Fig. 3.

Based on the above analysis, the oxidation mechanism of TBBPA/S in the FeCu@GF-2.0/PDS and FeCu@GF-2.0/PDS systems was proposed. Within the FeCu@GF-2.0/PDS system, PDS was adsorbed on the FeCu@GF-2.0 surface, forming a PDS* complex. Then, the charge on the hydroxyl group of TBBPA/S was transferred to the PDS* complex, leading to the oxidation of TBBPA/S. Within the FeCu@GF-2.0/PMS system, PMS was similarly adsorbed on the surface of FeCu@GF-2.0 to form a PMS* complex, and the metal atoms of FeCu@GF-2.0 in the low-valence state became high-valent metals due to the higher activity of PMS*, which electrophilically attacks the hydroxyl group of TBBPA/S.

3.5 Recyclability and application of FeCuS@GF-2.0

3.5.1 Recyclability of FeCuS@GF-2.0. The recyclability of FeCuS@GF-2.0 was evaluated over five consecutive cycles in

both the PDS and the PMS systems (Fig. S23). After five cycles of reactions, the removal efficiency of TBBPS in the FeCuS@GF-2.0/PDS system decreased significantly, while those in the FeCuS@GF-2.0/PMS system were still above 90%. This result may be due to the different reaction mechanisms within the PDS and PMS systems. In the FeCuS@GF-2.0/PDS system, the electron transfer process was the main pathway for the TBBPS degradation, suggesting that the adsorption of TBBPS on the surface of FeCuS@GF-2.0 was the key factor due to the accumulation of reaction intermediates on the catalyst surface, which blocked active sites and hindered the electron transfer process. The oxidation of thiophene S during the reaction is also considered to be one of the reasons for the decrease in degradation efficiency. However, after thermal regeneration *via* calcination, the catalytic performance was restored, confirming that surface fouling was the primary cause of deactivation (Fig. S23a). In the FeCuS@GF-2.0/PMS system, Fe(IV) species were the primary active species, which could efficiently degrade TBBPS. Since Fe(IV) species were the primary active species in the PMS system, rather than direct electron transfer, the reaction was less dependent on surface adsorption, indicating that the FeCuS@GF-2.0/PMS system has excellent stability and recyclability.

3.5.2 Application in actual soils. The effectiveness of FeCuS@GF-2.0 in real soil systems was evaluated using eight representative soil samples collected from different regions across China. The physicochemical properties of eight soils are presented in Table S1. The degradation efficiencies of TBBPA/S in the PDS- and PMS-alone systems are shown in Fig. S24a and b. In the PDS-alone system, the degradation efficiency of TBBPA in JX and CQ soils were 39.38% and 24.08%, respectively, while in other soils, efficiencies were below 20%. This difference can be attributed to the higher total Fe content of JX and CQ compared to the other soils, which could effectively activate PDS.[74,75] However, the degradation efficiencies of TBBPS by PDS in all soils were below 20%, suggesting that PDS alone was insufficient for effective TBBPS removal. The degradation efficiencies of TBBPA/S in the PMS-alone system were higher than those in the PDS-alone system, demonstrating the superior degradation performance of PMS across all soils. For example, in HLG, the degradation efficiencies of TBBPA by PDS and PMS were 0% and 24.05%, respectively, and those of TBBPS were 0% and 50.81%, respectively. Notably, in NX, the degradation efficiencies of TBBPA and TBBPS by PMS reached 78.77% and 92.54%, respectively. This enhanced removal in NX may be attributed to the alkaline conditions, which facilitate PMS activation.[76]

The change in pH before and after the reaction was used to determine the potential correlation between soil pH and the degradation efficiency of TBBPA/S. A negative ΔpH (the difference in soil pH before and after reaction) was observed in all tested soils (Fig. S24c), attributed to the acidity of PDS and PMS.[77] Although the final pH values varied slightly, no drastic changes were observed due to the natural buffering capacity of soils. The ΔpH values of the corresponding soils in the PMS-alone system were higher than those in the PDS-alone system, suggesting that PMS is significantly more acidic than PDS. Additionally, slight reductions in persulfate concentrations were observed after the reaction (Fig. S24), suggesting some level of persulfate activation by soil components.[77]

To further determine the impact of soil properties on individual PDS or PMS systems, a correlation analysis was conducted between removal efficiencies and soil properties. Since the removal efficiencies of TBBPA and TBBPS in the PDS-alone system were both below 20%, correlation analysis in the PDS-alone system was excluded. In the PMS-alone system, the higher removal efficiency of NX did not conform to normality, so it was excluded from correlation analysis. The results of the Shapiro–Wilk test showed that the TBBPA/S removal efficiencies and the partial properties of the tested soils were in line with normality. Therefore, Pearson correlation coefficient analysis was performed on the parameters that met normality, and the correlation coefficients are shown in Fig. S25. The correlation coefficients for TBBPA removal efficiencies with soil pH, free Fe content and total Fe content were −0.776, 0.968, and 0.806, respectively. The significant correlation coefficients for free Fe content with soil pH and total Fe content were −0.793 and 0.785, suggesting that higher free Fe content might be present in acidic soils.[78] These results suggested that free Fe content might be the key factor in the effective activation of PMS in soil.

In addition, the TBBPS removal efficiency was negatively correlated with soil pH (−0.869), consistent with the results of TBBPA. Moreover, the TBBPS removal efficiency was positively correlated with clay content (<0.002 mm, 0.825) and soil organic matter content (0.814). Soil clay particles, mainly including montmorillonite, kaolinite, illite and metal minerals, have high adsorption properties and catalytic activity.[79] Previous studies suggested that soil organic matter competes with target pollutants for active species,[80,81] resulting in lower removal efficiencies of target pollutants. However, recent studies found that persulfate could react with the phenoxy fraction of soil organic matter to produce a certain amount of reducing agent,[82,83] and TBBPS, as a typical halogenated compound, could be reduced by the reducing agent, resulting in the removal of TBBPS. A significant positive correlation coefficient (0.780) was found between the TBBPS removal efficiency and the amorphous Fe content. Amorphous Fe, as a highly active metallic mineral in soil, could effectively activate PMS.[84]

Degradation experiments of TBBPA/S in the FeCuS@GF-2.0/PDS or FeCuS@GF-2.0/PMS system were performed in eight soils. As shown in Fig. 7, the addition of FeCuS@GF-2.0 promoted the removal efficiencies of TBBPA/S in the tested soils. Compared with the PDS- or PMS-alone system (Fig. S24), the removal efficiencies of TBBPA/S in tested soils increased significantly with the addition of FeCuS@GF-2.0. However, the removal efficiencies of TBBPA/S in the tested soils were significantly lower than those under liquid phase conditions (Fig. 4). The underperformance of non-radical oxidation pathways in soil systems may be attributed to the following

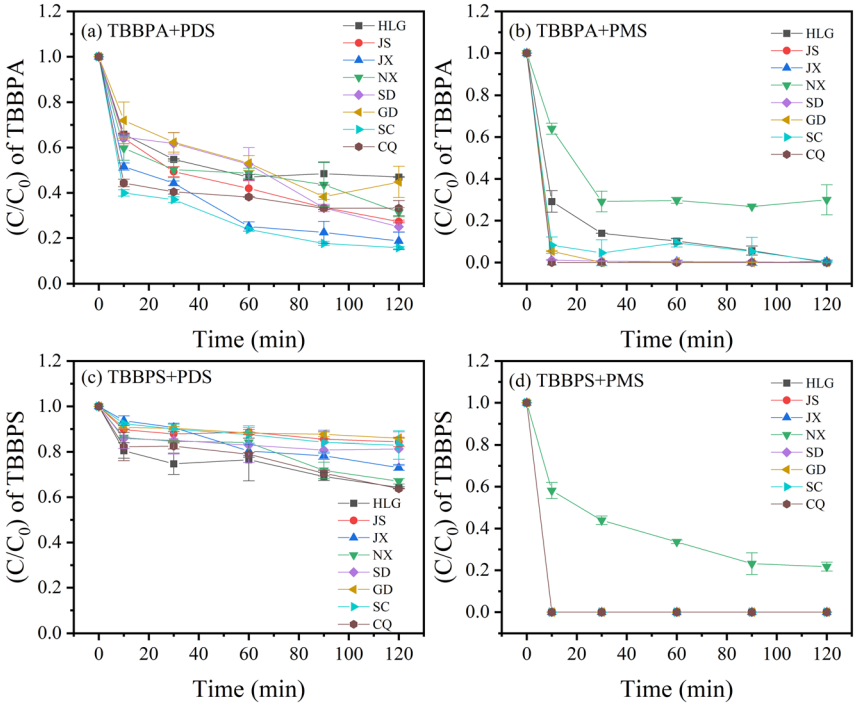

Fig. 7 The degradation efficiencies of (a) TBBPA and (c) TBBPS for all soils in the FeCuS@GF-2.0/PDS system. The degradation efficiencies of (b) TBBPA and (d) TBBPS for all soils in the FeCuS@GF-2.0/PMS system. Experimental conditions: [TBBPA] = [TBBPS] = 200 mg kg^{-1}, [PDS] = 0.5 mM, [PMS] = 0.1 mM.

reasons: (1) the soil–water partition coefficient of TBBPA/S. Due to the octanol–water partition coefficients ($\log K_{ow}$) of TBBPA/S being 6.53 and 5.2,[85] respectively, TBBPA/S tends to adsorb onto soil. The non-radical pathway can quickly oxidize TBBPA/S in the aqueous phase, so the desorption process of TBBPA/S from soil might inhibit non-radical oxidation in soil. (2) Competitive mechanism of soil organic matter (SOM). SOM contains a large amount of organic compounds, some of which are electron-rich organic compounds that may compete with TBBPA/S for non-radical active species,[86] inhibiting the non-radical oxidation pathway in soil. (3) Consumption of PDS/PMS by soil minerals. Soil minerals have been demonstrated to activate PDS/PMS to generate free radicals,[87] which are more easily consumed by SOM, reducing the FeCuS@GF-2.0-induced non-radical oxidation pathway and lowering the capacity for non-radical oxidation. Except for NX, 100% of TBBPA/S was removed within 90 min in the FeCuS@GF-2.0/PMS system (Fig. 7b and d). Compared with the PMS alone system, the FeCuS@GF-2.0/PMS system reduced the removal of TBBPA/S in NX by 9.2% and 13.9%, respectively, which might be attributed to the inhibition of the reaction process by the high pH of NX, consistent with the results of the aqueous-phase experiments (Fig. S9b and d). The FeCuS@GF-2.0/PMS system showed higher removal rates than the FeCuS@GF-2.0/PDS system on TBBPA/S, suggesting that the Fe(IV) oxidation pathway is more applicable to soil systems than the electron transfer pathway. The adsorption of target pollutants and persulfate on the catalyst surface was an important prerequisite for the electron transfer pathway.[51,88] Soil could adsorb the target pollutants,[89] but the organic matter in the soil competed with the target pollutants for the adsorption sites on the catalyst, which impeded the application of the electron transfer process in the soil systems. The degradation efficiency and reaction rate constants (k_{obs}) reported in the literature were compared with those in this study (Table S7). The results showed that a persulfate system based on the free radical or non-radical oxidation pathway could effectively remove organic pollutants in soil. The degradation efficiency of the non-radical oxidation pathway in this study is higher than that reported in other literature, suggesting that the selectivity of the non-radical oxidation pathways was an advantage over the free radical oxidation pathway.

3.5.3 Effect of soil physicochemical properties. To explore the influence of soil physicochemical properties on the FeCuS@GF-2.0/persulfate system, a correlation analysis was conducted between the net degradation efficiency (the removal efficiency in the FeCuS@GF-2.0/persulfate system minus that in the persulfate-alone system) and soil properties. The results of the Shapiro–Wilk test showed that net degradation efficiency and the partial properties of the tested soils were in line with normality. Therefore, Pearson correlation coefficient analysis was performed on the parameters that met normality, and the correlation coefficients are shown in Fig. S26. The net degradation efficiency of TBBPA in the FeCuS@GF-2.0/PDS system was positively correlated with the soil pH (0.741) (Fig. S26a). The increasing of soil pH could induce the ionization of TBBPA to produce $TBBPA^{2-}$, increasing its concentration in the aqueous phase, which facilitated the electron-transfer oxidation

of TBBPA on the surface of FeCuS@GF-2.0. As shown in Fig. S26b, the net degradation efficiency of TBBPS in the FeCuS@GF-2.0/PDS system was not significantly correlated with the physicochemical properties of the soils, which might be due to the lower removal of TBBPS by the electron transfer process. The net degradation efficiency of TBBPA in the FeCuS@GF-2.0/PMS system was also positively correlated with the soil pH (0.772), while the net degradation efficiency was negatively correlated with the free Fe (−0.967) and total Fe contents (−0.805) (Fig. S26c). Iron-containing minerals in the soil are effective activators of PMS, consuming PMS and thus inhibiting the production of Fe(IV).[90–92] The correlation coefficients for the net degradation efficiency of TBBPS in the FeCuS@GF-2.0/PMS system with soil pH, organic matter content, clay content (<0.002 mm), and amorphous Fe content were 0.869, −0.814, −0.825, and −0.780, respectively. The effect of soil pH and amorphous Fe content on TBBPS was similar to that on TBBPA (Fig. S26c). The increasing clay content may enhance the adsorption of TBBPS by soil,[93] thus inhibiting the adsorption of TBBPS on the FeCuS@GF-2.0 surface. In addition, soil organic matter could consume the active species and adsorb the target contaminants,[94,95] inhibiting the degradation of the target contaminants. In general, the effect of soil properties on the FeCuS@GF-2.0/persulfate system was related not only to soil pH, iron-containing mineral content, organic matter content, and clay content but also to the active species in the system.

4. Conclusions

In this study, recoverable FeCuS@GF-2.0 was prepared using a surface growth technique, and the reaction mechanism and influencing factors were investigated in advanced oxidation water treatment and actual soil treatment. FeCuS@GF-2.0 effectively activated PDS and PMS to degrade TBBPA/S in both water and soil. DFT calculations demonstrated that TBBPA was more prone to electrophilic attacks in comparison to TBBPS, so TBBPS should be considered more carefully as a broad alternative to TBBPA. Under optimal conditions (PDS = 0.5 mM), TBBPA was observed to be completely removed from water within 40 min, while the removal efficiency of TBBPS was 73.2% within 90 min. When PMS = 0.1 mM, 100% of TBBPA in water was removed within 30 min, while the complete removal of TBBPS took 90 min. The comprehensive experiments on active species showed that FeCuS@GF-2.0 could activate PDS and PMS to produce non-radical oxidation pathways with the electron transfer process and Fe(IV) as the principal active species, respectively. The removal rate of TBBPA/S in soil slurry was found to be significantly lower than that in aqueous solution. Furthermore, the degradation rate of TBBPA/S in the FeCuS@GF-2.0/PMS system was higher than that in the FeCuS@GF-2.0/PDS system, indicating that the non-radical oxidation pathway based on Fe(IV) was more suitable for soil remediation. The findings of correlation analyses demonstrated that soil pH was a common factor affecting the electron transfer process pathway and Fe(IV) oxidation pathway. Notably, Fe-containing minerals could affect the Fe(IV) oxidation pathway. These findings suggested that not only the soil properties but also the pollutant types should be considered in the actual soil application of non-radical oxidation pathways. This study provides a novel perspective on the application of non-radical oxidation pathways in soil and groundwater remediation. Future study will focus on how to adjust the non-radical oxidation pathway to reduce the impact of soil physical and chemical properties on pollutant degradation.

Author contributions

Qi Wang: conceptualization, formal analysis, methodology, supervision, validation, visualization, writing – original draft, and writing – review and editing. Xuewen Guo: resources, software, writing – review and editing. Aiguo Gu: funding acquisition, resources, software. Hongzhen Lian: conceptualization, resources, software, writing – review and editing. Jie Zou: funding acquisition, resources, software, writing – review and editing.

Conflicts of interest

The authors declare no competing interests.

Data availability

Supplementary information: The SI includes details of materials and methods, characterization of FeCuS@GFs material, results on the catalytic performance of FeCuS@GFs, results on active species, characterization of used FeCuS@GFs, and correlation analysis between soil properties and degradation efficiency. See DOI: **https://doi.org/10.1039/D5EN00600G**.

The authors declare that the data supporting the findings of this study are available within the paper. Should any raw data files be needed in another format, they are available from the corresponding author upon reasonable request.

Acknowledgements

This study has been supported by the Science and Technology Program of Jiangsu Provincial Administration for Market Regulation (No. KJ2024003), the Science and Technology Program of State Administration for Market Regulation (No. 2024MK043), the National Natural Science Foundation of China (No. 22176085, No. 21874065) and the Jiangsu Funding Program for Excellent Postdoctoral Talent.

References

1 A. Liu, J. Shi, Z. Shen, Y. Lin, G. Qu, Z. Zhao and G. Jiang, Identification of Unknown Brominated Bisphenol S Congeners in Contaminated Soils as the Transformation Products of Tetrabromobisphenol S Derivatives, *Environ. Sci. Technol.*, 2018, **52**, 10480–10489.

2 H. Zhou, N. Yin and F. Faiola, Tetrabromobisphenol A (TBBPA): A controversial environmental pollutant, *J. Environ. Sci.*, 2020, **97**, 54–66.

3 B. Zhu, G. Zhao, L. Yang and B. Zhou, Tetrabromobisphenol A caused neurodevelopmental toxicity via disrupting thyroid hormones in zebrafish larvae, *Chemosphere*, 2018, **197**, 353–361.
4 A. Nakajima, D. Saigusa, N. Tetsu, T. Yamakuni, Y. Tomioka and T. Hishinuma, Neurobehavioral effects of tetrabromobisphenol A, a brominated flame retardant, in mice, *Toxicol. Lett.*, 2009, **189**, 78–83.
5 T. Hurd and M. M. Whalen, Tetrabromobisphenol A decreases cell-surface proteins involved in human natural killer (NK) cell-dependent target cell lysis, *J. Immunotoxicol.*, 2011, **8**, 219–227.
6 X. Xu, Y. Zhang, H. Huang, J. Chen and T. Shi, Distribution, transformation, and toxic effects of the flame retardant tetrabromobisphenol S and its derivatives in the environment: A review, *Sci. Total Environ.*, 2024, **948**, 174799.
7 A. Li, T. Zhuang, W. Shi, Y. Liang, C. Liao, M. Song and G. Jiang, Serum concentration of bisphenol analogues in pregnant women in China, *Sci. Total Environ.*, 2020, **707**, 136100.
8 Z. Shi, Y. Jiao, Y. Hu, Z. Sun, X. Zhou, J. Feng, J. Li and Y. Wu, Levels of tetrabromobisphenol A, hexabromocyclododecanes and polybrominated diphenyl ethers in human milk from the general population in Beijing, China, *Sci. Total Environ.*, 2013, **452–453**, 10–18.
9 F. Chen, X.-T. Huang, C.-W. Bai, Z.-Q. Zhang, P.-J. Duan, Y.-J. Sun, X.-J. Chen, B.-B. Zhang and Y.-S. Zhang, Advancements in heterogeneous activation of persulfates: Exploring mechanisms, challenges in organic wastewater treatment, and innovative solutions, *Chem. Eng. J.*, 2024, **481**, 148789.
10 G. R. Peyton, The free-radical chemistry of persulfate-based total organic carbon analyzers, *Mar. Chem.*, 1993, **41**, 91–103.
11 S. Yang, P. Wang, X. Yang, L. Shan, W. Zhang, X. Shao and R. Niu, Degradation efficiencies of azo dye Acid Orange 7 by the interaction of heat, UV and anions with common oxidants: Persulfate, peroxymonosulfate and hydrogen peroxide, *J. Hazard. Mater.*, 2010, **179**, 552–558.
12 G. P. Anipsitakis, D. D. Dionysiou and M. A. Gonzalez, Cobalt-Mediated Activation of Peroxymonosulfate and Sulfate Radical Attack on Phenolic Compounds. Implications of Chloride Ions, *Environ. Sci. Technol.*, 2006, **40**, 1000–1007.
13 Y. Zhao, L. Yu, C. Song, Z. Chen, F. Meng and M. Song, Selective Degradation of Electron-Rich Organic Pollutants Induced by CuO@Biochar: The Key Role of Outer-Sphere Interaction and Singlet Oxygen, *Environ. Sci. Technol.*, 2022, **56**, 10710–10720.
14 X. Zhang, M. Fang, Z. Ning, Q. Wei, H. Guo, M. An, Q. Ma, J. Zhou and T. Wang, Efficient decomposition and mineralization of sulfadiazine by freezing/periodate via non-radical pathways decreased iodinated disinfection byproduct formation, *Sep. Purif. Technol.*, 2025, **377**, 134454.
15 X. Duan, H. Sun, Z. Shao and S. Wang, Nonradical reactions in environmental remediation processes: Uncertainty and challenges, *Appl. Catal., B*, 2018, **224**, 973–982.
16 Y. Song, S. Zhi, H. Wang, Q. Yang, J. Guo, C. Yang, K. Jiang and D. Wu, Laser-induced growth of metal oxide films on quartz tubes for photocatalytic water treatments, *Chem. Eng. J.*, 2024, **495**, 152895.
17 F. Zeng, Y. Feng, J. Wang, Y. Lin, R. Xiong, D. Wu and C. Yang, Insight into the structure-dependent effects of metal residues in conjugated polymers, *Chem. Commun.*, 2025, **61**, 9626–9629.
18 H. Wang, S. Wang, J. Li, S. Zhi, Y. Liu, K. Jiang, C. Yang and D. Wu, A tale of two boron sites in g-C3N4: Pulse laser-assisted modification and enhanced 2e− preferences for photocatalytic H2O2 production, *Chem. Eng. J.*, 2025, **510**, 161862.
19 Y. Wang, Y. Lin, C. Yang, S. Wu, X. Fu and X. Li, Calcination temperature regulates non-radical pathways of peroxymonosulfate activation via carbon catalysts doped by iron and nitrogen, *Chem. Eng. J.*, 2023, **451**, 138468.
20 H. Wang, W. Xu, X. Chen, Q. Yang, C. Shen, B. Zhang, Y. Lin, J. Sun, L. Zhang, Q. Zhang, Z. Lu and L. Chen, Transformation from a non-radical to a radical pathway: Via the amorphization of a Ni(OH)2catalyst as a peroxymonosulfate activator for the ultrafast degradation of organic pollutants, *Nanoscale*, 2021, **13**, 7700–7708.
21 J. Wang, J. Yao, Y. Li, Z. Wei, C. Gao, L. Jiang and X. Wu, S vacancies-introduced chalcopyrite switch radical to non-radical pathways via peroxymonosulfate activation: Vital roles of S vacancies, *J. Hazard. Mater.*, 2024, **467**, 133751.
22 Z. Wan, Y. Cao, Z. Xu, X. Duan, S. Xu, D. Hou, S. Wang and D. C. W. Tsang, Revealing Intrinsic Relations Between Cu Scales and Radical/Nonradical Oxidations to Regulate Nucleophilic/Electrophilic Catalysis, *Adv. Funct. Mater.*, 2023, **33**(12), 2212227.
23 D. Zhou, Z. Li, X. Hu, L. Chen and M. Zhu, Single Atom Catalyst in Persulfate Oxidation Reaction: From Atom Species to Substance, *Small*, 2024, **20**, 2311691.
24 K.-Y. A. Lin, Z.-Y. Zhang and T. Wi-Afedzi, Sulfur-doped carbon nitride as a non-metal heterogeneous catalyst for sulfate radical-based advanced oxidation processes in the absence of light irradiation, *J. Water Process Eng.*, 2018, **24**, 83–89.
25 J. Wang, K. Zhang, T. T. T. Nga, Y. Wang, Y. Shi, D. Wei, C.-L. Dong and S. Shen, Chalcogen heteroatoms doped nickel-nitrogen-carbon single-atom catalysts with asymmetric coordination for efficient electrochemical CO2 reduction, *Chin. J. Catal.*, 2024, **64**, 54–65.
26 Y. Pan, Y. Chen, K. Wu, Z. Chen, S. Liu, X. Cao, W.-C. Cheong, T. Meng, J. Luo, L. Zheng, C. Liu, D. Wang, Q. Peng, J. Li and C. Chen, Regulating the coordination structure of single-atom Fe-NxCy catalytic sites for benzene oxidation, *Nat. Commun.*, 2019, **10**, 4290.
27 L.-Z. Miao, Y.-X. Guo, Z.-Y. Liu, Y. Li, J. Zhu and L. Wu, High-entropy alloy nanoparticles/biochar as an efficient catalyst for high-performance treatment of organic pollutants, *Chem. Eng. J.*, 2023, **467**, 143451.
28 Z. Lai, Y. Yang, Z. Yang, W. Ruan, C. Yang, Q. Chen, K. Ding, J. Zhang and Y. Hou, Carbon nitride grafted with single-atom manganese and 2-hydroxy-4,6-dimethylpyrimidine: A visible-light-driven photocatalyst for enhanced ozonation of organic pollutants, *J. Colloid Interface Sci.*, 2025, **683**, 1106–1118.

29 H. J. Yu, R. Shi, Y. X. Zhao, T. Bian, Y. F. Zhao, C. Zhou, G. I. N. Waterhouse, L. Z. Wu, C. H. Tung and T. R. Zhang, Alkali-Assisted Synthesis of Nitrogen Deficient Graphitic Carbon Nitride with Tunable Band Structures for Efficient Visible-Light-Driven Hydrogen Evolution, *Adv. Mater.*, 2017, **29**, 1605148.

30 P. Zhang, D. Sun, A. Cho, S. Weon, S. Lee, J. Lee, J. W. Han, D. P. Kim and W. Choi, Modified carbon nitride nanozyme as bifunctional glucose oxidase-peroxidase for metal-free bioinspired cascade photocatalysis, *Nat. Commun.*, 2019, **10**, 940.

31 X. Li, J. Wang, X. Duan, Y. Li, X. Fan, G. Zhang, F. Zhang and W. Peng, Fine-Tuning Radical/Nonradical Pathways on Graphene by Porous Engineering and Doping Strategies, *ACS Catal.*, 2021, **11**, 4848–4861.

32 B. Xu, H. Wang, W. Wang, L. Gao, S. Li, X. Pan, H. Wang, H. Yang, X. Meng, Q. Wu, L. Zheng, S. Chen, X. Shi, K. Fan, X. Yan and H. Liu, A Single-Atom Nanozyme for Wound Disinfection Applications, *Angew. Chem., Int. Ed.*, 2019, **58**, 4911–4916.

33 D. Ding, S. Yang, X. Qian, L. Chen and T. Cai, Nitrogen-doping positively whilst sulfur-doping negatively affect the catalytic activity of biochar for the degradation of organic contaminant, *Appl. Catal., B*, 2020, **263**, 118348.

34 M. Qiao, X. F. Wu, S. Zhao, R. Djellabi and X. Zhao, Peroxymonosulfate enhanced photocatalytic decomposition of silver-cyanide complexes using g-C3N4 nanosheets with simultaneous recovery of silver, *Appl. Catal., B*, 2020, **265**, 118587.

35 P. Yang, S. Zuo, F. Zhang, B. Yu, S. Guo, X. Yu, Y. Zhao, J. Zhang and Z. Liu, Carbon Nitride-Based Single-Atom Cu Catalysts for Highly Efficient Carboxylation of Alkynes with Atmospheric CO2, *Ind. Eng. Chem. Res.*, 2020, **59**, 7327–7335.

36 J. Liu, T. Zhang, Z. Wang, G. Dawson and W. Chen, Simple pyrolysis of urea into graphitic carbon nitride with recyclable adsorption and photocatalytic activity, *J. Mater. Chem.*, 2011, **21**, 14398–14401.

37 H. Liu, P. Sun, M. Feng, H. Liu, S. Yang, L. Wang and Z. Wang, Nitrogen and sulfur co-doped CNT-COOH as an efficient metal-free catalyst for the degradation of UV filter BP-4 based on sulfate radicals, *Appl. Catal., B*, 2016, **187**, 1–10.

38 X. Chen, W.-D. Oh and T.-T. Lim, Graphene- and CNTs-based carbocatalysts in persulfates activation: Material design and catalytic mechanisms, *Chem. Eng. J.*, 2018, **354**, 941–976.

39 H. Li, C. Shan and B. Pan, Fe(III)-Doped g-C3N4 Mediated Peroxymonosulfate Activation for Selective Degradation of Phenolic Compounds via High-Valent Iron-Oxo Species, *Environ. Sci. Technol.*, 2018, **52**, 2197–2205.

40 J. Ma, N. Jia, C. Shen, W. Liu and Y. Wen, Stable cuprous active sites in Cu(+)-graphitic carbon nitride: Structure analysis and performance in Fenton-like reactions, *J. Hazard. Mater.*, 2019, **378**, 120782.

41 Z. Zhao, W. Zhou, D. Lin, L. Zhu, B. Xing and Z. Liu, Construction of dual active sites on diatomic metal (FeCo –N/C-x) catalysts for enhanced Fenton-like catalysis, *Appl. Catal., B*, 2022, **309**, 121256.

42 G. Liang, Z. Yang, Z. Wang, X. Cai, X. Zhang and X. Xie, Relying on the non-radical pathways for selective degradation organic pollutants in Fe and Cu co-doped biochar/peroxymonosulfate system: The roles of Cu, Fe, defect sites and ketonic group, *Sep. Purif. Technol.*, 2021, **279**, 119697.

43 Z. Chen, L. Wang, H. Xu and Q. Wen, Efficient heterogeneous activation of peroxymonosulfate by modified CuFe2O4 for degradation of tetrabromobisphenol A, *Chem. Eng. J.*, 2020, **389**, 124345.

44 P. Neta, R. E. Huie and A. B. Ross, Rate Constants for Reactions of Inorganic Radicals in Aqueous Solution, *J. Phys. Chem. Ref. Data*, 1988, **17**, 1027–1284.

45 Y. Gao, Z. Chen, Y. Zhu, T. Li and C. Hu, New Insights into the Generation of Singlet Oxygen in the Metal-Free Peroxymonosulfate Activation Process: Important Role of Electron-Deficient Carbon Atoms, *Environ. Sci. Technol.*, 2020, **54**, 1232–1241.

46 Y. Li, T. Yang, S. Qiu, W. Lin, J. Yan, S. Fan and Q. Zhou, Uniform N-coordinated single-atomic iron sites dispersed in porous carbon framework to activate PMS for efficient BPA degradation via high-valent iron-oxo species, *Chem. Eng. J.*, 2020, **389**, 124382.

47 S. Mostafa and F. L. Rosario-Ortiz, Singlet Oxygen Formation from Wastewater Organic Matter, *Environ. Sci. Technol.*, 2013, **47**, 8179–8186.

48 X. X. Pan, J. Chen, N. N. Wu, Y. M. Qi, X. X. Xu, J. L. Ge, X. H. Wang, C. G. Li, R. J. Qu, V. K. Sharma and Z. Y. Wang, Degradation of aqueous 2,4,4'-Trihydroxybenzophenone by persulfate activated with nitrogen doped carbonaceous materials and the formation of dimer products, *Water Res.*, 2018, **143**, 176–187.

49 P. Bilski, K. Reszka, M. Bilska and C. F. Chignell, Oxidation of the spin trap 5,5-dimethyl-1-pyrroline N-oxide by singlet oxygen in aqueous solution, *J. Am. Chem. Soc.*, 1996, **118**, 1330–1338.

50 S. Zhu, X. Huang, F. Ma, L. Wang, X. Duan and S. Wang, Catalytic Removal of Aqueous Contaminants on N-Doped Graphitic Biochars: Inherent Roles of Adsorption and Nonradical Mechanisms, *Environ. Sci. Technol.*, 2018, **52**, 8649–8658.

51 W. Ren, L. Xiong, X. Yuan, Z. Yu, H. Zhang, X. Duan and S. Wang, Activation of Peroxydisulfate on Carbon Nanotubes: Electron-Transfer Mechanism, *Environ. Sci. Technol.*, 2019, **53**, 14595–14603.

52 W. Ren, L. Xiong, G. Nie, H. Zhang, X. Duan and S. Wang, Insights into the Electron-Transfer Regime of Peroxydisulfate Activation on Carbon Nanotubes: The Role of Oxygen Functional Groups, *Environ. Sci. Technol.*, 2020, **54**, 1267–1275.

53 B. Yang and G.-G. Ying, Oxidation of benzophenone-3 during water treatment with ferrate(VI), *Water Res.*, 2013, **47**, 2458–2466.

54 W. H. Koppenol and J. F. Liebman, The oxidizing nature of the hydroxyl radical. A comparison with the ferryl ion (FeO2+), *J. Phys. Chem.*, 1984, **88**, 99–101.

55 T. V. Popova and N. V. Aksenova, Complexes of Copper in Unstable Oxidation States, *Russ. J. Coord. Chem.*, 2003, **29**, 743–765.

56 L. Wang, H. Xu, N. Jiang, Z. Wang, J. Jiang and T. Zhang, Trace Cupric Species Triggered Decomposition of Peroxymonosulfate and Degradation of Organic Pollutants: Cu(III) Being the Primary and Selective Intermediate Oxidant, *Environ. Sci. Technol.*, 2020, **54**, 4686–4694.

57 Y. Wang, Y. Wu, Y. Yu, T. Pan, D. Li, D. Lambropoulou and X. Yang, Natural polyphenols enhanced the Cu(II)/peroxymonosulfate (PMS) oxidation: The contribution of Cu(III) and HO·, *Water Res.*, 2020, **186**, 116326.

58 X. Liu, P. Xu, Q. Fu, R. Li, C. He, W. Yao, L. Wang, S. Xie, Z. Xie, Q. He and J. C. Crittenden, Ferric ion promoted degradation of acetaminophen with zero − valent copper activated peroxymonosulfate process, *Chem. Eng. J.*, 2021, **426**, 131679.

59 B. Dey, Y. S. Jain and A. L. Verma, Infrared and Raman spectroscopic studies of KHSO4 crystals, *J. Raman Spectrosc.*, 1982, **13**, 209–212.

60 A. Goypiron, J. De Villepin and A. Novak, Raman and infrared study of KHSO4 crystal, *J. Raman Spectrosc.*, 1980, **9**, 297–303.

61 Q. Wang, D. Zhou, C. Liu, X. Chen, L. Liu and K. Lin, Enhancing effect of dual-atom catalysts on tetrabromobisphenol S degradation via peroxydisulfate activation: Synergism of Fe–Cu and electron-transfer mechanism, *Chem. Eng. J.*, 2023, **460**, 140681.

62 B. Huang, Z. Wu, X. Wang, X. Song, H. Zhou, H. Zhang, P. Zhou, W. Liu, Z. Xiong and B. Lai, Coupled Surface-Confinement Effect and Pore Engineering in a Single-Fe-Atom Catalyst for Ultrafast Fenton-like Reaction with High-Valent Iron-Oxo Complex Oxidation, *Environ. Sci. Technol.*, 2023, **57**, 15667–15679.

63 M. Huang, X. Wang, C. Liu, G. Fang, J. Gao, Y. Wang and D. Zhou, Facile ball milling preparation of sulfur-doped carbon as peroxymonosulfate activator for efficient removal of organic pollutants, *J. Environ. Chem. Eng.*, 2021, **9**, 106536.

64 X. Duan, Z. Ao, L. Zhou, H. Sun, G. Wang and S. Wang, Occurrence of radical and nonradical pathways from carbocatalysts for aqueous and nonaqueous catalytic oxidation, *Appl. Catal., B*, 2016, **188**, 98–105.

65 P. Shao, J. Tian, F. Yang, X. Duan, S. Gao, W. Shi, X. Luo, F. Cui, S. Luo and S. Wang, Identification and Regulation of Active Sites on Nanodiamonds: Establishing a Highly Efficient Catalytic System for Oxidation of Organic Contaminants, *Adv. Funct. Mater.*, 2018, **28**, 1705295.

66 H. Li, J. Tian, F. Xiao, R. Huang, S. Gao, F. Cui, S. Wang and X. Duan, Structure-dependent catalysis of cuprous oxides in peroxymonosulfate activation via nonradical pathway with a high oxidation capacity, *J. Hazard. Mater.*, 2020, **385**, 121518.

67 Q. Ye, H. Xu, J. Zhang, Q. Wang, P. Zhou, Y. Wang, X. Huang, X. Huo, C. Liu and J. Lu, Enhancement of peroxymonosulfate activation for antibiotics removal by nano zero valent tungsten induced Cu(II)/Cu(I) redox cycles, *Chem. Eng. J.*, 2020, **382**, 123054.

68 Y. Wang, Z. Zhang, Z. Yin, Z. Liu, Y. Liu, Z. Yang and W. Yang, Adsorption and catalysis of peroxymonosulfate on carbocatalysts for phenol degradation: The role of pyrrolic-nitrogen, *Appl. Catal., B*, 2022, **319**, 121891.

69 R. G. Parr and W. Yang, Density functional approach to the frontier-electron theory of chemical reactivity, *J. Am. Chem. Soc.*, 1984, **106**, 4049–4050.

70 C. Morell, A. Grand and A. Toro-Labbé, New Dual Descriptor for Chemical Reactivity, *J. Phys. Chem. A*, 2005, **109**, 205–212.

71 X. Wang, Z. Xiong, H. Shi, Z. Wu, B. Huang, H. Zhang, P. Zhou, Z. Pan, W. Liu and B. Lai, Switching the reaction mechanisms and pollutant degradation routes through active center size-dependent Fenton-like catalysis, *Appl. Catal., B*, 2023, **329**, 122569.

72 Q. Ji, K. Du, J. Zhu, X. Ye, H. Li, X. Cheng, Y. Liu, Z. Xu, G. Zuo, S. Li, S. Yang, L. Zhang and H. He, Acid-tailored self-assembled perylene diimide supramolecular for visible-light-driven activation of peroxymonosulfate towards efficient degradation of iohexol, *Chem. Eng. J.*, 2023, **462**, 142116.

73 P. Politzer and J. S. Murray, in *Rev. Comput. Chem.*, 1991, pp. 273–312, DOI: **10.1002/9780470125793.ch7**.

74 M. Usman, P. Faure, C. Ruby and K. Hanna, Application of magnetite-activated persulfate oxidation for the degradation of PAHs in contaminated soils, *Chemosphere*, 2012, **87**, 234–240.

75 N. Yan, F. Liu, Q. Xue, M. L. Brusseau, Y. Liu and J. Wang, Degradation of trichloroethene by siderite-catalyzed hydrogen peroxide and persulfate: Investigation of reaction mechanisms and degradation products, *Chem. Eng. J.*, 2015, **274**, 61–68.

76 C. Qi, X. Liu, J. Ma, C. Lin, X. Li and H. Zhang, Activation of peroxymonosulfate by base: Implications for the degradation of organic pollutants, *Chemosphere*, 2016, **151**, 280–288.

77 Y. Chen, C. Yan, Y. Zhang, L. Qiu and M. Nie, Natural soil as the peroxymonosulfate activator for efficient remediation and detoxification of bisphenol A: Nonradical-dominated mechanism and the change of soil properties, *Chem. Eng. J.*, 2024, **491**, 152043.

78 B. T. Oba, X. Zheng, M. A. Aborisade, A. Kumar, A. Y. Battamo, J. Liu, A. A. Laghari, P. Sun, Y. Yang and L. Zhao, Application of KHSO5 for remediation of soils polluted by organochlorides: A comprehensive study on the treatment's efficacy, environmental implications, and phytotoxicity, *Sci. Total Environ.*, 2023, **871**, 162023.

79 N. Chen, G. Fang, C. Zhu, S. Wu, G. Liu, D. D. Dionysiou, X. Wang, J. Gao and D. Zhou, Surface-bound radical control rapid organic contaminant degradation through peroxymonosulfate activation by reduced Fe-bearing smectite clays, *J. Hazard. Mater.*, 2020, **389**, 121819.

80 J. Wu, M. Zhuang, Z. Zou, J. Xin, F. Wang, C. Jia and H. Zhang, Efficient degradation of clothianidin and thiamethoxam in contaminated soil by peroxymonosulfate process, *Environ. Sci. Pollut. Res.*, 2023, **30**, 48211–48219.

81 J. Deng, Y. Ge, C. Tan, H. Wang, Q. Li, S. Zhou and K. Zhang, Degradation of ciprofloxacin using α-MnO2 activated peroxymonosulfate process: Effect of water constituents, degradation intermediates and toxicity evaluation, *Chem. Eng. J.*, 2017, **330**, 1390–1400.

82 M. Ahmad, A. L. Teel and R. J. Watts, Mechanism of Persulfate Activation by Phenols, *Environ. Sci. Technol.*, 2013, **47**, 5864–5871.

83 M. Yu, A. L. Teel and R. J. Watts, Activation of Peroxymonosulfate by Subsurface Minerals, *J. Contam. Hydrol.*, 2016, **191**, 33–43.

84 X. Zhang, D. D. Gang, X. Lei, T. Wang, Q. Lian, W. E. Holmes, L. Fei, M. E. Zappi and H. Yao, Surface-bound hydroxyl radical-dominated degradation of sulfamethoxazole in the amorphous FeOOH/peroxymonosulfate system: The key role of amorphous structure enhancing electron transfer, *Environ. Res.*, 2022, **214**, 113964.

85 H. Kuramochi, K. Kawamoto, K. Miyazaki, K. Nagahama, K. Maeda, X. W. Li, E. Shibata, T. Nakamura and S. Sakai, Determination of physicochemical properties of tetrabromobisphenol A, *Environ. Toxicol. Chem.*, 2008, **27**, 2413–2418.

86 X. Dong, X. Yang, S. Hua, Z. Wang, T. Cai and C. Jiang, Unraveling the mechanisms for persulfate-based remediation of triphenyl phosphate-contaminated soils: Complicated soil constituent effects on the formation and propagation of reactive oxygen species, *Chem. Eng. J.*, 2021, **426**, 130662.

87 J. Liang, X. Duan, X. Xu, Z. Zhang, J. Zhang, L. Zhao, H. Qiu and X. Cao, Critical Functions of Soil Components for In Situ Persulfate Oxidation of Sulfamethoxazole: Inherent Fe(II) Minerals-Coordinated Nonradical Pathway, *Environ. Sci. Technol.*, 2024, **58**, 915–924.

88 H. Wang, W. Guo, B. Liu, Q. Si, H. Luo, Q. Zhao and N. Ren, Sludge-derived biochar as efficient persulfate activators: Sulfurization-induced electronic structure modulation and disparate nonradical mechanisms, *Appl. Catal., B*, 2020, **279**, 119361.

89 W. Han, L. Luo and S. Zhang, Adsorption of tetrabromobisphenol A on soils: Contribution of soil components and influence of soil properties, *Colloids Surf., A*, 2013, **428**, 60–64.

90 C. Liu, Enhancement of dewaterability and heavy metals solubilization of waste activated sludge conditioned by natural vanadium-titanium magnetite-activated peroxymonosulfate oxidation with rice husk, *Chem. Eng. J.*, 2019, **359**, 217–224.

91 M. Yang, X. Ren, L. Hu, W. Guo and J. Zhan, Facet-controlled activation of persulfate by goethite for tetracycline degradation in aqueous solution, *Chem. Eng. J.*, 2021, **412**, 128628.

92 Q. Qin, T. Liu, J. Zhang, R. Wei, S. You and Y. Xu, Facile synthesis of oxygen vacancies enriched α-Fe2O3 for peroxymonosulfate activation: A non-radical process for sulfamethoxazole degradation, *J. Hazard. Mater.*, 2021, **419**, 126447.

93 F. Tong, X. Gu, C. Gu, R. Ji, Y. Tan and J. Xie, Insights into tetrabromobisphenol A adsorption onto soils: Effects of soil components and environmental factors, *Sci. Total Environ.*, 2015, **536**, 582–588.

94 K. Chen, J. Liang, X. Xu, L. Zhao, H. Qiu, X. Wang and X. Cao, Roles of soil active constituents in the degradation of sulfamethoxazole by biochar/persulfate: Contrasting effects of iron minerals and organic matter, *Sci. Total Environ.*, 2022, **853**, 158532.

95 X. Tang, M. Z. Hashmi, B. Zeng, J. Yang and C. Shen, Application of iron-activated persulfate oxidation for the degradation of PCBs in soil, *Chem. Eng. J.*, 2015, **279**, 673–680.